Numerical modelling of long flexible fibers in homogeneous isotropic turbulence*

Mostafa Sulaiman[1], Eric Climent[1,a], Blaise Delmotte[1,b], Pascal Fede[1], Franck Plouraboué[1], and Gautier Verhille[2]

[1] Institut de Mécanique des Fluides de Toulouse (IMFT) Université de Toulouse, CNRS-INPT-UPS, F-31400 Toulouse, France
[2] Aix Marseille Univ, CNRS, Centrale Marseille, IRPHE, Marseille, France

Abstract. We numerically investigated the transport, deformation and buckling events of an isolated elas-tic fiber in Taylor-Green vortices and studied the dynamics of long filaments in homogeneous isotropic turbulence. The fiber is modelled by an assembly of spherical beads. The contact between beads enforces the inextensibility of the filament while bending is accounted for by the Gears Bead Model (GBM) pro-posed by Delmotte *et al.* (2015). In the cellular Taylor-Green flow, the buckling probability is a function of a dimensionless number, called Sperm number, which is a balance between the compression rate of the flow and the elastic response of the filament. The shapes of the filament and its ability to buckle have been successfully validated through comparisons with experiments from the work by Quennouz *et al.* (2015). The deformation statistics of long flexible fibers in sustained homogeneous isotropic turbulence were analyzed for various flow and fiber material conditions. Two regimes have been identified depending on the ratio of fiber length to persistence length which is a measure of turbulent forcing to flexibility. The numerical results are in good agreement with existing experimental data (C. Brouzet *et al.*, Phys. Rev. Lett. **112**, 074501 (2014)) validating the assumptions of our model for the configurations we investigated.

1 Introduction

1.1 Context

When a highly elongated solid object, like a thin rod or a filament, moves in a fluid, its ability to bend depends on the interplay between its material properties and the flow forcing. Drag, strain, and pressure gradient can generate strong deviations of the object from its initial shape. This is commonly observed in environmental flows such as wheat in the blade bending under the wind and elongated algae in the ocean [1]. In industrial applications, it is observed in wood filaments in papermaking industry [2], fibers to strengthen composite materials, textile and food industry. In human body, it appears through DNA actin filaments and fibrine. Microfluidic engineering and biotechnologies are also concerned with flow-induced deformation of flexible filaments. Fiber deformation and its relation to spatial dispersion has an important role on the overall response of polymer suspensions undergoing the coil-stretch transition. For concentrated suspensions of fibers like in wood pulp, the effect of fiber flexibility on the rheology is still an open question due to the complexity induced by fiber deformation and entanglement leading to the formation of flocs.

1.2 Literature overview

A vast literature exists on the response of suspensions of solid spherical or non-spherical particles, such as oblate, prolate or thin rods. When objects have the ability to deform, many complications arise. The coupling between suspended particles will depend on the positions (possibly orientations) but also on the shape of individuals, introducing intricate effects of the history of the suspension. Many previous investigations of fiber dynamics, have focused on the dynamics of rigid fibers or rods [3,4]. The questions which have been addressed are the orientation dynamics and preferential orientation of non-spherical objects in homogeneous [5] or wall-bounded turbulence [6]. Compared to the very large number of references related to particle suspensions, lower attention

* Contribution to the Topical Issue "Flowing Matter, Problems and Applications", edited by Federico Toschi, Ignacio Pagonabarraga Mora, Nuno Araujo, Marcello Sega.

[a] e-mail: `eric.climent@imft.fr` (corresponding author)
[b] *Present address*: LadHyX, UMR CNRS 7646, Ecole Polytechnique, 91128 Palaiseau CEDEX, France.

has been paid to the more complicated systems of flexible fibers in a turbulent fluid [7]. Polymer physics is a vast field of research on flexible filament dynamics. More specifically, drag reduction by dilute concentrations of long-chain polymer molecules has proven to be very efficient in turbulent regime. The phenomenon is known for many years [8] although the physical understanding of such drastic reduction of momentum flux in a wall-bounded shear flow is still under investigation [9]. The configuration of homogeneous isotropic turbulence is a generic flow configuration to disentangle the respective effects of the mean shear and turbulent structures [10] on the stretching and relaxation of long polymer chains.

Understanding the dynamics of flexible fibers in complex configurations such as a turbulent flows is of primary interest. Wandersman *et al.* [11] studied experimentally fiber deformation and transport in a viscous cellular flow created by a lattice of magnets in an electrolyte. They found that compressive viscous stress could be responsible for the buckling of elastic fibers. They analyzed the effect of fiber deformation on its translational motion and measured the buckling threshold in agreement with the linear stability analysis for a purely hyperbolic flow. The same phenomenon was investigated by [12] and [13]. Quennouz *et al.* [13] compared their numerical simulations with the experimental results of [11] on the transport, buckling and dynamics of an elastic isolated fiber in 2D cellular vortex flow. They specifically investigated the buckling probability while varying the elasto-viscous number $\mathtt{Sp}$. Fiber dynamics were studied experimentally in turbulent flows by [14] for fibers of different lengths and mechanical properties. A model for the evolution of the time average end-to-end vector was proposed for the transition from rigid to flexible regime as the intensity of turbulence is varied.

In the present work, we study fiber deformation in two fluid flow configurations. In the first configuration, we investigate fiber deformation and buckling events in the Taylor-Green vortex flow and we compare our results to the experiments and simulations of [11,12] and [13]. We consider this as a validation of our model in a simplistic turbulence model. In the second configuration, we investigate the deformation of fibers in homogeneous isotropic turbulence. We first detail the numerical modelling of fiber deformation and its coupling with the carrying flow, where we couple the Gears Bead Model (GBM) proposed in [15] with Direct Numerical Simulations of the Navier-Stokes equations. The one-way coupling accounts only for the effect of fluid flow on fiber without taking in account the effect of fiber on the flow. In our approach, we use a first step to include part of the two-way coupling through the Rotne-Prager-Yamakawa mobility tensor. Nevertheless, we only account for local hydrodynamic interactions between neighboring beads of the fiber and do not consider interactions over longer distances.

2 Numerical model

Simulating flexible fiber deformations can be handled by different approaches from the slender body theory to the full simulation of fluid-structure interactions based on a solution of the Navier-Stokes equations with no-slip boundary conditions on a deformable surface. Although we are interested in turbulence flow regimes where fluid inertia is important, for neutrally buoyant filaments low Reynolds assumption is a good approximation of local flow around a fiber as there is no slip due to gravity and local slip is only due to the fiber elastic response. In the context of Stokesian dynamics, a number of approaches have been developed, such as resistive force theory and boundary integral elements. We here adopt a bead model, thoroughly described and validated in [15].

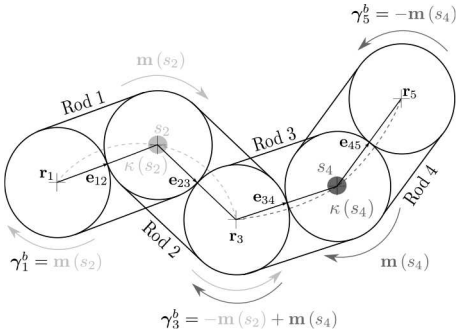

Fig. 1. Fiber discretization and bending torques acting on beads. The fiber is composed of spherical beads which stay in contact through no-slip rolling conditions. Two consecutive beads are forming a rod.

2.1 Gears Bead Model (GBM)

The GBM discretizes any flexible slender body into a set of interacting beads, fig. 1 [15]. Kinematic constraint forces related to the inextensiblility are included in the model together with hydrodynamic forcing and elastic response.

Thus, the transport and deformation of the filament depends on forces and torques applied on each bead. The elastohydrodynamics of homogeneous flexible and inextensible fiber is considered. The fiber is decomposed into a set of objects which experience bending torques and elastic forces to recover their equilibrium shape, the bending moments derivation and discretization are described below. Then, the role of bending moments and constraint forces is addressed in the force and torque balance for the assembly.

The constitutive law giving the bending moment, $\mathbf{m}(s)$, of an elastic beam reads

$$\mathbf{m}(s) = K^b \mathbf{t} \times \frac{\mathrm{d}\mathbf{t}}{\mathrm{d}s}\,, \tag{1}$$

where K^b(s) is the bending rigidity, $\mathbf{t}$ is a unit vector tangent along the beam centerline and s is the curvilinear abscissa. Using the Frenet-Serret formula

$$\frac{\mathrm{d}\mathbf{t}}{\mathrm{d}s} = \kappa(s)\,\mathbf{n} \tag{2}$$

the bending moment could be written as

$$\mathbf{m}(s) = K^b\,\kappa(s)\,\mathbf{b}, \tag{3}$$

where $\kappa(s)$ is the local curvature, $\mathbf{n}$ and $\mathbf{b}$ are the normal and bi-normal unit vectors of the Frenet-Serret frame of reference. We consider that the beam is discretized into N rigid beads of diameter $d = 2a$. Inextensible fibers are made up of two bond beads and linked together by a flexible joint with bending rigidity K^b. Bending moments are evaluated at joint locations $s_i = (i-1)\lambda$ for $i = 2, \ldots, N-1$ where s_i corresponds to the curvilinear abscissa of the mass center of the i-th bead. In the following discrete unit vectors connecting the center of mass of bead $i-1$ to the center of mass of bead i are denoted using the Frenet-Serret triad associated with tangent, normal and binormal $(\mathbf{t}_i, \mathbf{n}_i, \mathbf{b}_i)$. The local curvature $\kappa(s_i)$ can then be estimated from a first-order discretization of arc-length along the fiber, eq. (2), projected onto the normal $\mathbf{n}$:

$$\kappa(s_i) = \frac{1}{2a}\left(\mathbf{t}_{i+1} - \mathbf{t}_i\right) \cdot \mathbf{n}_i = \frac{1}{2a}\mathbf{t}_{i+1} \cdot \mathbf{b}_i \times \mathbf{t}_i. \quad (4)$$

Thus this leads to the following formulation of the discrete curvature, as in [16]:

$$\kappa(s_i) = \frac{1}{2a}\left(\mathbf{t}_i \times \mathbf{t}_{i+1}\right) \cdot \mathbf{b}_i, \quad (5)$$

where $\mathbf{b}_i = \mathbf{t}_i \times \mathbf{n}_i = \frac{\mathbf{t}_i \times \mathbf{t}_{i+1}}{\|\mathbf{t}_i \times \mathbf{t}_{i+1}\|}$ and $\kappa(s_i) = \frac{1}{2a}\|\mathbf{t}_i \times \mathbf{t}_{i+1}\|$.

The bending torque on bead i is then given by eq. (6). We show the torque computation on a beam discretized with five beads in fig. 1:

$$\boldsymbol{\gamma}_i^b = \mathbf{m}(s_{i+1}) - \mathbf{m}(s_{i-1}). \quad (6)$$

This elementary geometric law [16] provides an approximation of the curvature $\kappa(s_i)$ when the angle between two adjacent tangent vectors is small. Contact forces determined by Lagrange multipliers ensure the connectivity and inextensiblity conditions since it is derived from the rolling contact kinematic constraints. It circumvents the use of spring forces between adjacent bead. Hence, this represents a huge saving of numerical cost, since there is no need for small time-stepping resulting from the use of stiff potentials.

2.2 Hydrodynamic coupling

In our beads model, the fiber is composed of spherical particles to account for the finite width of its cross-section. The hydrodynamic interactions are provided through the solution of the mobility problem which relates forces and torques to the translational and rotational velocities of the beads. This many-body problem is non-linear in the instantaneous positions of all particles of the system. Approximate solutions of this complex mathematical problem can be achieved by limiting the mobility matrices to their leading order. Pairwise interactions are required to account for anisotropic drag effects within the beads composing the fiber. We use the Rotne-Prager-Yamakawa (RPY) tensor for the determination of buckling probability of fibers in Taylor-Green vortex flow, one of the most commonly used approximation to include hydrodynamic interactions. We use a simpler model for fibers in turbulence, called free drain, as the mobility matrix is assumed to be diagonal through neglecting hydrodynamic interactions with neighboring spheres. We perform a one-way coupling that does not account for fiber effect on fluid, as previously performed in the studies of [12] and [13]. Long-range hydrodynamic interactions might become important when the fiber is so coiled that it is near self-contacting or forming knots, *i.e.* when the length of the fiber is very large. We consider only neutrally buoyant filaments, thus ignoring gravity effects. In the first part, the flow field is analytically specified by the Taylor-Green solution that is an exact solution of two-dimensional steady Navier-Stokes equations. For the second part, we solve the three-dimensional Navier-Stokes equations

$$\rho_f \frac{D\mathbf{u}}{Dt} = -\nabla p + \mu \nabla^2 \mathbf{u} + \mathbf{f}, \quad (7)$$

$$\nabla \cdot \mathbf{u} = 0, \quad (8)$$

where $\mathbf{u}$, is the instantaneous fluid velocity, p the pressure, $\mathbf{f}$ the large scale forcing to sustain turbulence, ρ the fluid density and μ the dynamic viscosity. The solution is time advanced using a third-order Adams-Bashforth scheme. The computational domain is a cubic box of dimensions $(2\pi)^3$ with tri-periodic boundary conditions. The Fourier pseudo-spectral method is used to solve momentum balance and continuity equations. Statistically stationary turbulence was sustained by applying homogeneous, isotropic, time-correlated forcing [17] over a narrow shell of small wavenumbers, $\mathbf{f}$ in eq. (8), which produces integral-scale fluid fluctuations (*i.e.*, the size of the largest eddies) on the order of one-tenth of the domain size. We calculated turbulent flows for two different Taylor Reynolds numbers, ranging from 51 to 97, by varying the number of mesh points from 128^3 to 512^3 to ensure that the Kolmogorov scale was fully resolved in each case. In all simulations, the separation between forcing and dissipation scales was sufficient to produce the universal characteristics of a homogeneous isotropic turbulent flow. The fluid velocity is linearly interpolated at the particle centers of beads composing a fiber assuming their radius to be small compared to the smallest eddies corresponding typically ten Kolmogorov length scales.

2.3 Numerical setting

The particles are tracked using a mesh-less method by integrating the equations of motion using a 3rd-order Adams-Bashforth integration scheme. In the case of turbulent flows, the time step is determined by the stability condition for solving the Navier-Stokes equations. Depending on the fiber material properties, the time step to resolve fiber deformation can be larger or smaller than the time step for fluid flow resolution. We always consider the smallest of the two numerical conditions which possibly yields sub-stepping for the Gear Bead Model. The kinematics of the filament results from the cumulative contributions of individual bead motions. Positions are obtained

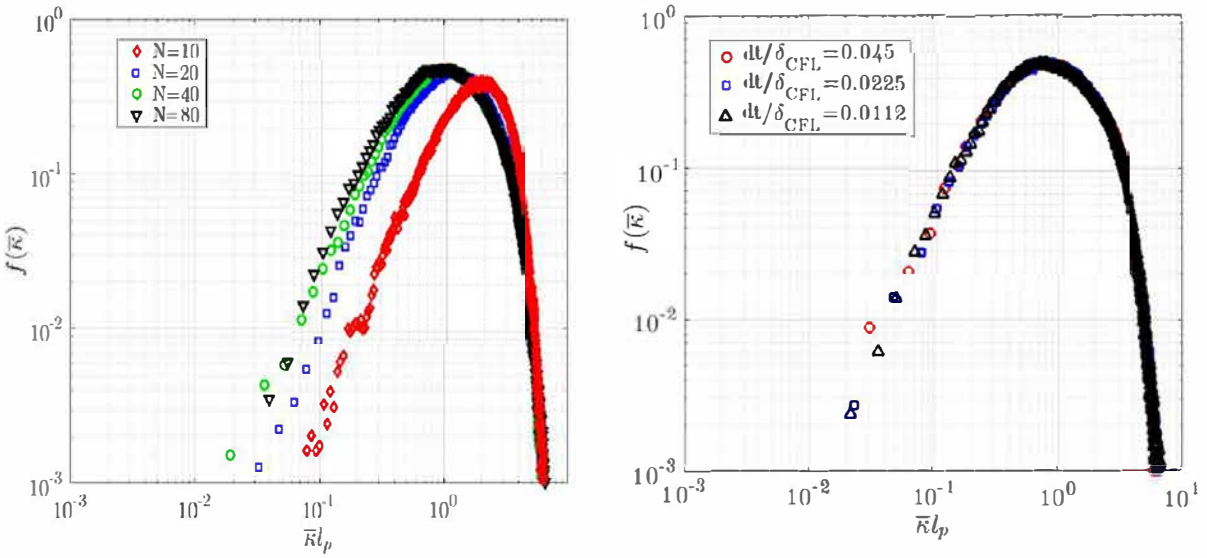

(a) (b)

Fig. 2. Probability density functions of the mean curvature (eq. (11)) of fibers in turbulence. (a) Effect of fiber discretization into N beads on the determination of the curvature. l_p is the persistence length defined in eq. (15). (b) Effect of the time step on the numerical solution with N=20. δ_{CFL} is the Courant-Friedrichs-Lewy reference time step.

from the temporal integration of the equation of motion with a 3rd-order Adams-Bashforth scheme

$$\frac{\mathrm{d}\mathbf{r}_i}{\mathrm{d}t} = \mathbf{v}_i, \tag{9}$$

where $\mathbf{r}_i$, $\mathbf{v}_i$ are the position and translational velocity of bead i. The time step Δt used to integrate eq. (9) is fixed by the characteristic bending time

$$\Delta t < \frac{\mu(2a)^4}{K^b} \quad \text{with } K^b = E\frac{\pi d^4}{64};$$
$$\Delta t < \frac{64\mu}{\pi E} \quad (E \text{ is the Young modulus}) \tag{10}$$

where μ is the fluid viscosity. K^b has the dimension of a force times a surface. Temporal convergence has been validated in fig. 2 where δ_{CFL} is the Courant-Friedrichs-Lewy reference time step based on the rms fluctuations of the flow velocity and the width of a mesh cell. The classic recommendation for numerical stability is to choose a time step corresponding to $\delta_{CFL}/20$ or lower.

The Frenet-Serret formula eq. (2) relates the fiber curvature and the bending moment which can be written as eq. (3) for discretization with N beads. The local curvature is defined between three consecutive beads. We statistically studied the fiber curvature as a local probe of turbulent forcing experienced by the filament. For this, the Probability Density Function (PDF) of the mean curvature is evaluated from eq. (11) as the algebraic mean curvature of the fiber. This provides a single value of the curvature $\overline{\kappa}$ at each time step:

$$\overline{\kappa} = \frac{1}{N-2}\sum_{i=2}^{N-1} |\kappa(s_i)|. \tag{11}$$

Table 1. Turbulent flow properties of the numerical simulations.

Flow type	I	II
Box size	$2\pi^3$	$2\pi^3$
Grid size	128^3	512^3
μ viscosity	10^{-3}	10^{-3}
η_k Kolmogorov length	0.0286	0.007
λ_g Taylor microscale	0.23	0.17
L_g integral scale	0.7	0.7
Re_λ Reynolds number	51	97
ϵ dissipation rate	0.0015	0.34
ρ_f density	1	1
Cores number	8	64
Δt time step	10^{-2}	2×10^{-4}

The discretization of the fiber with a finite set of beads requires their number to adequately describe the bending deformation of an elastic fiber. For this aim, we performed a set of numerical simulations by changing only the beads number N in a turbulent flow. A fiber of length $L = 2$ in a domain $2\pi^3$, rigidity $K^b = 10^{-6}$ inside flow type (I) (see table 1) was discretized with N = 10, 20, 40 and 80 beads. The PDFs of the mean curvature, defined by eq. (11), were plotted to evaluate the effect of discretization in fig. 2. We selected a case corresponding to very flexible fibers which is the most sensitive to the fiber discretization as strong bending events are often occurring.

This shows when the number of beads is insufficient, strong bending effects are flawed, corresponding to a lower probability of small curvature for ten beads discretization.

Increasing N to twenty, events of smaller curvature are more frequent. For $N = 40$ we find that the two curves of the PDF are almost overlapping which indicates the convergence of bead discretization. No much differences are observed with simulations corresponding to $N = 20$, 40 or 80. We consider that $N = 20$ is adequate for discretization.

3 Fibers in Taylor-Green flow

The Taylor-Green velocity field is described by eq. (12), where $\tilde{x} = \pi x/W$, $\tilde{y} = \pi y/W$ are the dimensionless Cartesian coordinates and W is the vortex width:

$$\mathbf{U} = U_0 \begin{pmatrix} \sin(\tilde{x})\cos(\tilde{y}) \\ -\cos(\tilde{x})\sin(\tilde{y}) \end{pmatrix}. \qquad (12)$$

Equation (12) corresponds to a two-dimensional periodic array of counter-rotating vortices. The ratio of the fiber length to the vortex width, $\alpha = L/W = 0.4$, is matching the experimental conditions of [13]. Initially fibers are randomly distributed and orientated throughout the flow. The problem is controlled by two dimensionless parameters, α and the Sperm number [18] $\mathtt{Sp} = \frac{\mu L^4 S}{K^b a^4}$, where μ is the fluid viscosity, L and a are, respectively, the fiber length and radius ($L/a = 12$), S is the compression rate and K^b is the bending modulus of the fiber. The Sperm number as defined above corresponds to the elasto-viscous number defined by [13]. In experiments, fibers are floating on the fluid-air surface but the effect of the meniscus has been shown to be negligible due to the size and material properties of the filament. We consider only neutrally buoyant filaments, thus ignoring gravity effects as fiber and fluid densities are constant and equal.

3.1 Fiber deformation

In our simulations, fibers are shown to be either captured within the vortices or translating along the backbone of the stable and unstable manifolds that are connecting the array of compression or extension regions. As the fiber approaches the surrounding of the stagnation point corresponding to compression region, it may buckle. Theoretically, buckling was explained by [12] as it arises from the instability of a nearly straight fiber under viscous compressive loading. This instability occurs beyond a critical strain rate of the linear flow and it is associated with a U-shaped deformation mode. In our simulations V-shaped, U-shaped and S-shaped fibers have been clearly observed for $\mathtt{Sp} = 450$. For higher $\mathtt{Sp}$ more deformation shapes occur and they are shown in fig. 3.

3.2 Statistics of buckling events

Hundreds of non-interacting fibers were simultaneously distributed inside the domain to achieve statistical convergence. Simulations were performed during 1000 time units (W/u_0) during which fiber beads positions are computed. The maximum value of $\mathtt{Sp}$ was about $1.4\ 10^4$ in previous studies. We extend the range up to $\mathtt{Sp} = 10^8$. A constant probability of buckling has been attained above $\mathtt{Sp} = 10^6$. A buckling event is defined as follows: the fiber enters a compression region in a non-coiled state, *i.e.* $R_{e,2D}/L > 0.8$, and buckles inside the compression region, *i.e.* $R_{e,2D}/L < 0.8$, where $R_{e,2D}$ is the end-to-end length of the fiber in two dimensions. Each time a fiber enters a compression region we add one to the number of trajectories N_{tracks}. The probability is given by the ratio of the number of buckling events N_{events} to the total number of trajectories passing through the compression regions, $P_{Buckling} = N_{events}/N_{tracks}$. If a fiber buckles more than once in the compression region we only consider the first buckling event. This procedure is similar to the experimental determination of the buckling probability used by [13]. We show in fig. 4 the evolution of buckling probability when Sperm number $\mathtt{Sp}$ is varied over eight decades.

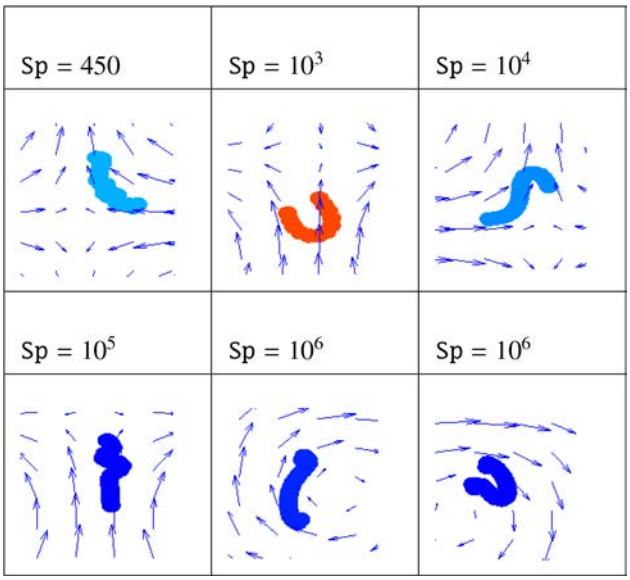

Fig. 3. Fiber shapes observed near the stagnation points or within vortices corresponding to Sperm number $\mathtt{Sp} \geq 450$.

Note that measurements are subject to statistical errors inversely proportional to $\sqrt{N_{events}}$ where N_{events} is the total number of buckling events for each $\mathtt{Sp}$. In our simulations, the error bars become smaller due to the large number of events we obtain by running simulations for a long time and inserting many non-interacting fibers simultaneously. The agreement of our simulations is very good when compared to both experiments and simulations of [13], carried out with a different numerical model.

4 Fibers in homogeneous isotropic turbulence

An experimental study was carried out by [14] to characterize, analyze and model fiber deformations in turbulence. The corresponding snapshots of the numerical simulations are shown in fig. 5. In experiments, neutrally buoyant fibers were inserted into flow confined in a

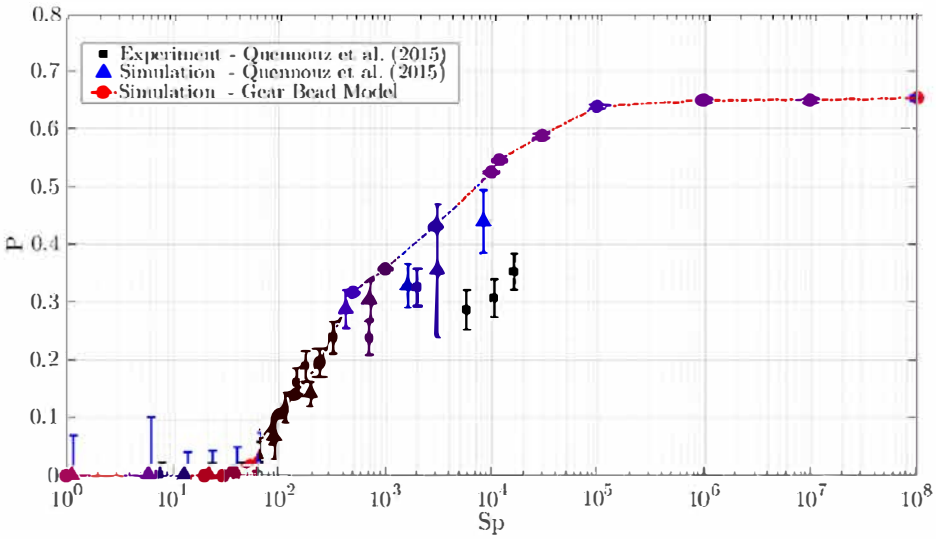

Fig. 4. Buckling probability *vs.* Sperm number. Red dots with dashed line correspond to buckling probability of our simulations, blue triangles correspond to buckling probability of ref. [13] simulations, and black squares correspond to their experiments.

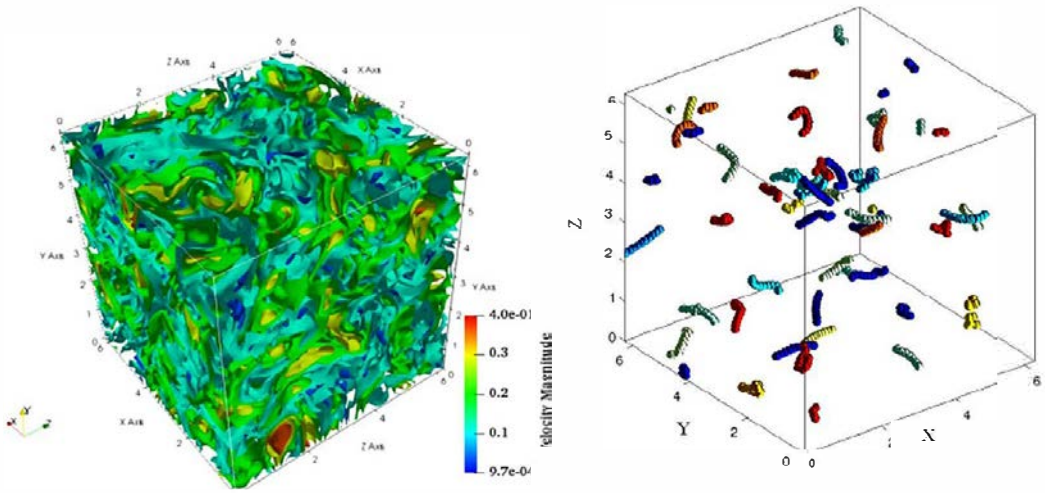

(a) (b)

Fig. 5. (a) Visualization of Homogeneous Isotropic Turbulence for $Re_\lambda = 51$ with velocity contours. (b) Snapshot of the fibers positions simulated in Homogeneous Isotropic Turbulence. The number of fibers is 45 with diameter $d = 0.1$ and length $L = 2$ discretized with 20 beads.

Table 2. Properties of fibers and carrying fluid in experiments.

Type		I
Material		Silicone
E	MPa	21
ρ	kg/m^3	1350
$2a$	μm	900
K^b	N · m^2	6.75×10^{-7}
L	cm	[1.1, 17.6]
μ	Pa · s	0.8×10^{-3}
ρ_f	kg/m^3	1000

cylinder of radius 8 cm and length 18 cm. The turbulent flow was driven by two counter-rotating disks separated by a distance with variable rotational frequency form 2 to 30 Hz, allowing to increase the integral Reynolds number form 10^5 to 1.4×10^6. The flexibility of the filament is varied by increasing the length of fiber for fixed bending modulus and diameter. Fiber properties are given in table 2. When turbulence production balances viscous dissipation, the Kolmogorov length scale $\eta_k = (\nu^3/\epsilon)^{1/4}$ can be determined from the rate of energy dissipation ϵ, or equivalently the injected power per unit mass. The rotational frequency and the injected power are related by the relation $\epsilon = (2\pi\beta)^3 R^2 F^3$, where R is the disk radius and $\beta = 0.1$ is a constant obtained experimentally. For each rotational frequency, flow scales change. Fibers length varies from 1 cm (rigid regime) up to 17.4 cm (flexible regime). All images are recorded far from the walls, in the center

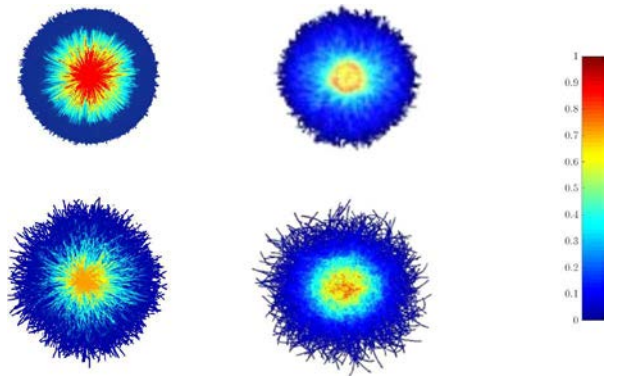

Fig. 6. Comparison between numerical simulations (left column) and experiments (right column) of fiber deformation for rigid regime (top row) and flexible regime (bottom row). Each fiber has one end positioned at the center of the graphic and color is proportional to the probability of finding one bead of the fiber at the considered position from the center.

of the cylinder where the flow is expected to be isotropic and homogeneous. The end-to-end vector $\mathbf{R}_{e,3D}$ connecting the two extremities of the fiber writes as

$$\mathbf{R}_{e,3D} = (\mathbf{X}_f - \mathbf{X}_o), \tag{13}$$

where $\mathbf{X}_o$ and $\mathbf{X}_f$ denote the absolute positions of the two extremities of the fiber. The experimental setup permits to capture snapshots of individual fibers. Image post-processing provides a 2D projection of the end-to-end vector. Because the end-to-end vector PDF shares the same symmetry as turbulence which is assumed to be rotationally invariant, a correction factor was used to adapt the measurements to 3D. For the numerical modelling, the end-to-end vector $\mathbf{R}_{e,3D} = \mathbf{X}_N - \mathbf{X}_1$ of the fiber discretized in N beads is used to characterize the evolution of the fiber normalized by its length L.

The deformations of fiber can be visualized experimentally by shifting the fiber's center of mass towards the center of flow whilst superposing $\mathbf{R}_{e,3D}$ and testing the isotropy of its radial distribution function for various regimes. Figure 6 is composed of the superposition of many instantaneous snapshots of the filament shape. One end of each fiber has been placed in the center of the graphic as a common origin of the accumulated filament shapes. For the rigid regime, short fiber as shown in fig. 6(top), the superposition was found to form a smooth sphere whereas for the flexible regime, shown in fig. 6(bottom), the superposition showed a sphere with a rough surface due to the fiber deformation. The comparison of experiments and numerical simulations shows a good agreement.

Changing the fiber length affects its flexibility which yields variations of its local curvature. For these two regimes, we compare in fig. 7 the probability density functions of simulations with theoretical predictions [19] and experimental data. For a rigid fiber of length L, the PDF follows the theoretical prediction $P_{Re^2} = 1/2L^2(1 - Re^2/L^2)^{-1/2}$ whereas in the flexible regime the PDF is Gaussian, $P_{Re^2} = \exp(-Re^2/\langle Re^2\rangle)/\langle Re^2\rangle$. Both predictions are in good agreement with the numerical simulations of rigid rods or long flexible fibers and associated experiments. The gyration radius is given by

$$R_g{}^2 = \frac{1}{N}\sum_{i=1}^{N} r_i^2, \tag{14}$$

where r_i is the bead's i perpendicular distance from the fiber's center of inertia. We plot the PDF of gyration radius for rigid and flexible cases. For the rigid case, the PDF shows a sharp peak slightly below the value of strictly rigid rods δ_R. In the case of long flexible filaments, the distribution of the gyration radius is much broader as a result of the deformation of fiber by the turbulent structures yielding successive stretch-coil events. This behavior is expected as the fiber length L is much smaller than the persistence length l_p, eq. (15), while the case corresponding to L much larger than l_p shows a PDF following an exponential decay. l_p defines the typical length over which bending is balancing flow-induced deformation. For an intermediate length, the PDF changes continuously from the rigid regime to Gaussian distribution:

$$l_p = (EI)^{1/4}/(\mu\rho\epsilon)^{1/8}. \tag{15}$$

4.1 Numerical results

The turbulent kinetic energy K, or turbulence fluctuations u', are obtained by averaging over space and time after the initial transient, two to three integral time scales are necessary to develop the statistically steady state of turbulence. This can be also evaluated in the spectral space by integrating the energy spectrum function $E(k)$ as

$$K = \frac{1}{2}\langle u_i' u_i'\rangle = \int_0^{k_{max}} E(k)\mathrm{d}k. \tag{16}$$

The rate of kinetic energy dissipation per unit volume, ϵ, is balanced by the volumetric power input of the turbulence forcing and it is directly evaluated by integration of the dissipation spectrum $D(k)$ over all wavenumbers:

$$\epsilon = \int_0^{k_{max}} D(k)\mathrm{d}k = 2\nu\int_0^{k_{max}} k^2 E(k)\mathrm{d}k, \tag{17}$$

where $\nu = \mu/\rho$ is the kinematic viscosity. The two typical length scales which characterize the turbulent fluid, are the Taylor microscale, $\lambda^2 = \frac{15\nu u'^2}{\epsilon}$, and the Kolmogorov length scale $\eta = (\frac{\nu^3}{\epsilon})^{\frac{1}{4}}$. The Reynolds number based on the Taylor microscale is defined as $Re_\lambda = u'\lambda/\nu$. L_g is the integral length scale of the turbulent flow whose properties are listed in table 1. The evolution of fiber deformation characterized by the vector $\mathbf{R}_{e,3D}$ is investigated numerically. A dimensionless number is used to compare the turbulence forcing to the elastic response of fiber. We define a turbulent Sperm number by balancing turbulent dissipation with the elastic property of the fiber:

$$\mathtt{Sp} = \frac{\rho\lambda^3\epsilon\mu\lambda^5}{(EI)^2} = \frac{\mu\rho\epsilon\lambda^8}{(EI)^2} = \frac{L^8}{l_p^8}\,. \tag{18}$$

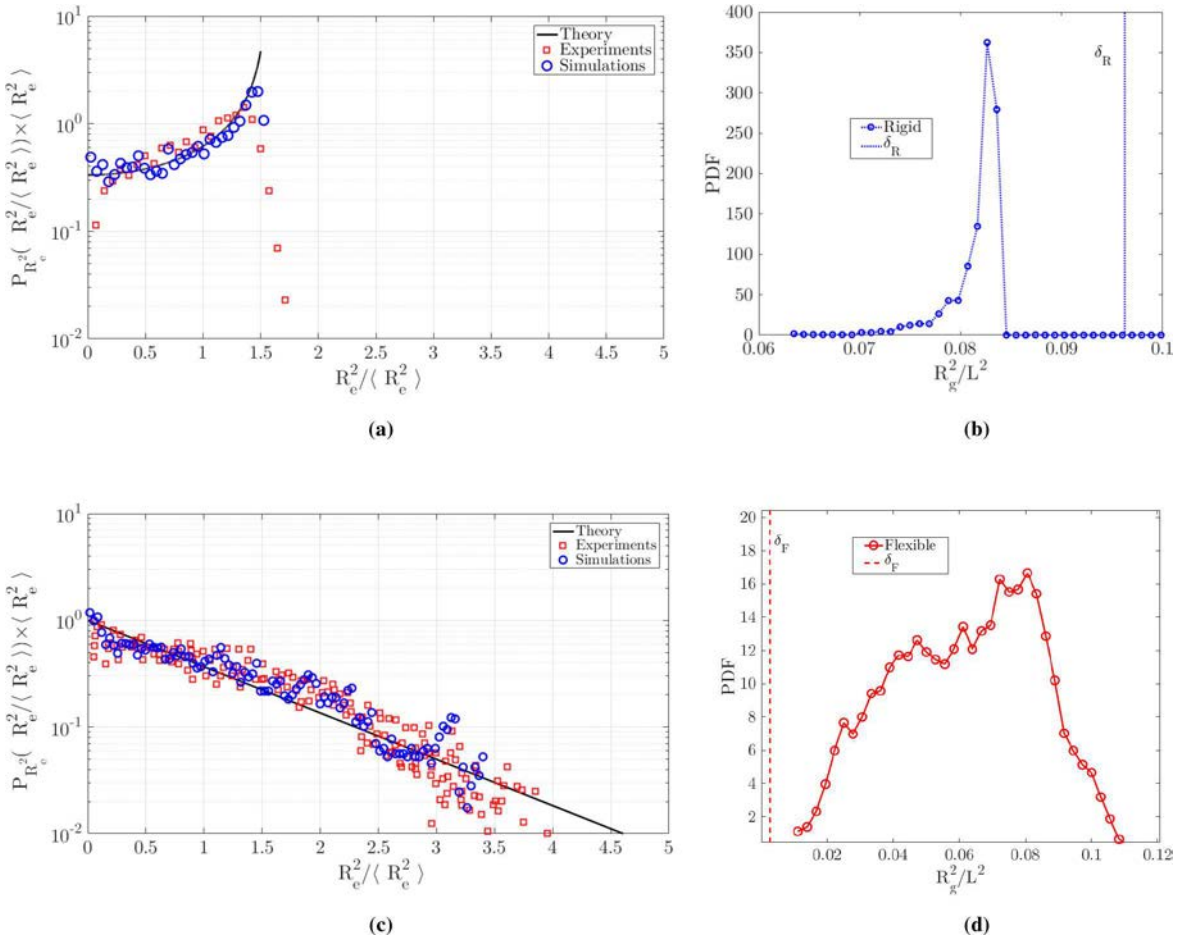

Fig. 7. Comparison between theoretical prediction, experimental and numerical results. (a) PDF of end-to-end distance for rigid fiber and (b) PDF of gyration radius for rigid fiber; $L = 1$, $K^b = 10^{-5}$ and flow type I. (c) PDF of end-to-end distance for flexible fiber and (d) PDF of gyration radius for flexible fiber; $L = 1.8$, $K^b = 40 \times 10^{-17}$ and flow type I. δ_R corresponds to straight rods while $\delta_F = 1/(6N)^{1/2}$ is the theoretical prediction for the entropically governed polymer chain following a random walk in three dimensions.

This can be interpreted as the ratio of a typical length scale of bending to fiber length. As fibers do not interact with each other neither with fluid, we insert hundreds of fibers into a box of volume $(2\pi)^3$ to achieve statistical convergence. Fibers are initially randomly distributed in positions and orientations. In experiments, one single fiber was used and statistics were formed over time. The gravitational force was neglected as the fiber density was close to that of surrounding fluid. We show the fibers properties in table 2.

Through simulations, fibers get deformed by the flow in a sustained turbulence. Fibers are randomly seeded throughout the whole domain of simulations with a straight shape. After a transient which ensures that fibers are statistically well deformed by the flow, the calculations of the $\mathbf{R}_{e,3D}$ vector is carried out by finding the end-to-end distance from the positions of the two beads at the extremities of the fiber. Two sets of flow configurations were simulated corresponding to an increase of the Reynolds number of the flow, table 1. This is experimentally equivalent to varying the rotational frequency of the disks. In each flow configuration, the length of fibers and material properties were widely varied to compare with experiments which were limited to a narrower range of variation. In both experiments and simulations, fiber material and length are chosen such that both rigid and flexible regimes are addressed for the turbulent flow configurations under consideration. The time average end-to-end squared vector $\langle \mathbf{R}^2_{e,3D} \rangle_t$ *vs.* fiber length has been measured experimentally for the rotational frequency $F = 20\,\mathrm{Hz}$. It is observed that the general behavior for the short and rigid fibers scales linearly, fig. 8, while long and flexible fibers deviate from $\langle \mathbf{R}^2_{e,3D} \rangle_t / L^2 = 1$ because fiber experiences turbulent forcing yielding to the local curvature of the beam and $\langle \mathbf{R}^2_{e,3D} \rangle_t < L^2$. The log-log plot gives the impression that the behavior is purely linear, although for long fibers the behavior is no longer linear. Therefore, for the long flexible fiber, an analogy with the worm-like chain model for a polymer was proposed by [14]. The predictions of the end-to-end vector were compared to the polymer model. It is determined by the persistence length for a thermally agitated polymer. The vector $\mathbf{R}_{e,3D}$ is predicted

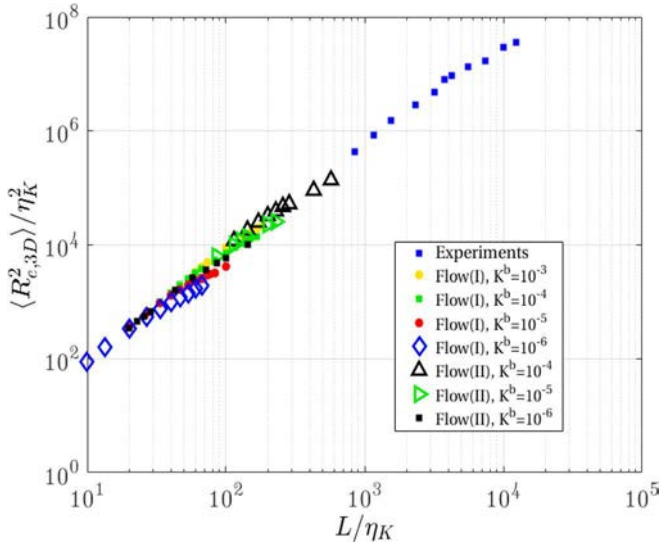

Fig. 8. Evolution of the end-to-end distance for fibers of different lengths L, bending rigidities K^b and flow parameters. $\langle \mathbf{R}^2_{e,3D}\rangle_t$ is scaled by the Kolmogorov length.

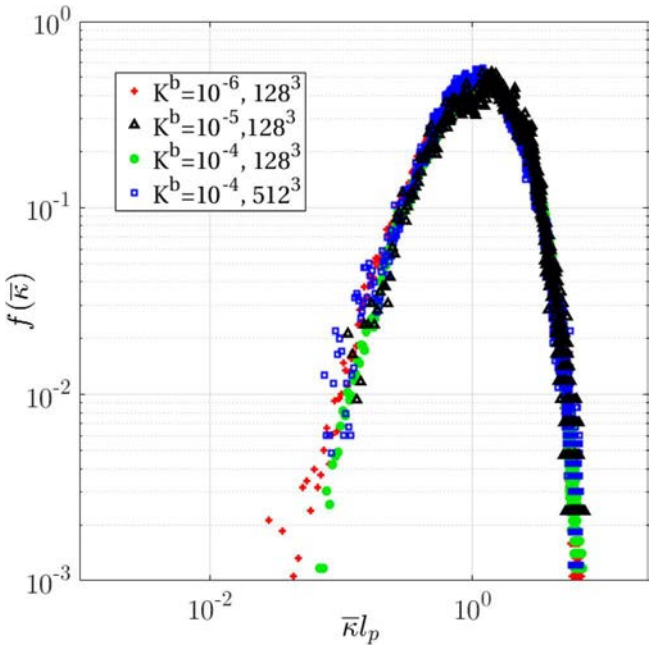

Fig. 9. Probability density functions of the mean curvature (eq. (11)) of fibers in turbulence for different flow parameters and fiber material properties.

by the following equation:

$$\langle \mathbf{R}^2_{e,3D}\rangle = \gamma\left(2\ell_p L - 2\ell_p^2\left[1-\exp\left(\frac{-L}{\ell_p}\right)\right]\right), \qquad (19)$$

where γ is a constant prefactor and ℓ_p is the persistence length representing the correlation length of the orientation along the chain. It is a basic mechanical property quantifying the stiffness of a polymer. The persistence length is expressed as $\ell_p = K^b/k_BT$ for polymers and l_p from eq. (18) for a fiber in turbulence. K^b is the bending modulus and k_BT is the thermal energy. For rigid fibers, $\langle \mathbf{R}^2_{e,3D}\rangle = L^2$ as $L \ll \ell_p$ whereas for long flexible fibers $\langle \mathbf{R}^2_{e,3D}\rangle = 2l_pL$ as $L \gg \ell_p$.

Figure 8 displays the log-log plot of $\langle \mathbf{R}^2_{e,3D}\rangle$ with dimensionless length to the Kolmogorov scale ratio L/η_K. This plot shows that, for the range of stiffness parameters we investigated, a flexible fiber scaling behavior $\langle \mathbf{R}^2_{e,3D}\rangle \sim L$ is mostly observed, which also favorably compares with the observed experimental trend. In fig. 8, the Kolmogorov length is chosen as a reference scale, for both the end-to-end distance of the chain and its total length. These results are somehow unexpected since given the flow type, and bending rigidity, the fiber is not always in the flexible regime. In order to more closely investigate this issue, we compute the evolution of the end-to end distance. The Sperm number associated with all the flow types and bending rigidity provided in fig. 10 does not only correspond to the flexible regime only, but also partly to the rigid one, for which this behavior is also consistent with the finding of fig. 9.

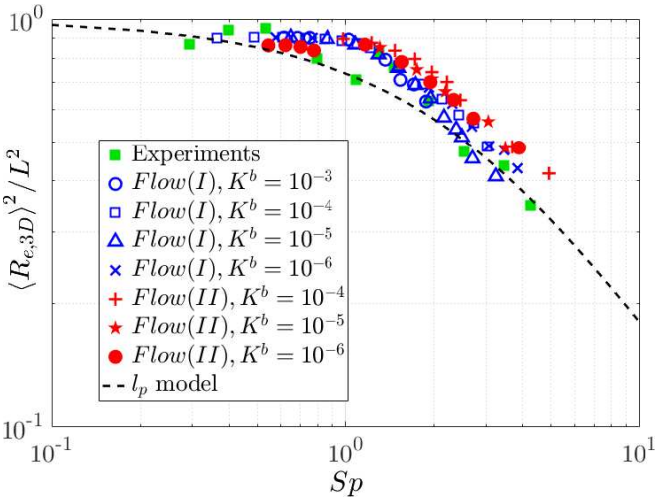

Fig. 10. Evolution of the dimensionless end-to-end distance with Sperm number. Comparison of $\langle \mathbf{R}^2_{e,3D}\rangle_t/L^2$ for simulations with $\gamma = 3$, experiments of [14] with $\gamma = 2$, and model of eq. (19) in dashed line.

4.2 Discussion

The squared vector $\langle \mathbf{R}^2_{e,3D}\rangle_t$ can characterize fiber deformation in fluctuating environment such as turbulence. In fig. 9, the mean curvature estimated from eq. (11) indicates that the persistence length $l_p = (\mu\rho\epsilon)^{1/8}/(EI)^{1/4}$ provides a consistent length scale for the fiber bending. All data corresponding to different bending modulus and two flow configurations collapse on a master curve only determined by the persistence length. This means that compressive deformation and elastic response are balanced to provide the characteristic bending scale. Moreover, this confirms the relevance of the choice made for the persis-

tence length as the relevant scale for fiber deformation or equivalently the Sperm number, which is deduced from the ratio between the fiber length and the persistence length l_p, consistently with Rosti *et al.* (2018).

When fiber length changes, the interaction with the flow changes because fiber is experiencing different eddy sizes and intensity corresponding to different rates of deformation resulting in variations of the local curvature. Rosti *et al.* [20] considered a continuous 1D, infinitely thin, inextensible elastic model for the fiber with isotropic drag and an Immersed Boundary Method (IBM) for fully coupled simulations. Based on scaling arguments, they considered the elastic/inertia balance to define a critical bending rigidity above which the time response of the fiber is either dominated by the turbulent eddies, or oppositely, beyond which, the flexible elastic response governs its dynamic. They suggested that the resulting end-to-end fiber statistics could be used to probe the turbulence statistics, especially in the second flexible regime where turbulence time-scale is smaller than the elastic relaxation time-scale. This balance is exactly the one provided by our Sperm number. Some differences in the analysis of the overdamped limit of the fiber elastic relaxation of [20] and previous publications also appear which are not explored here. Hence, when we focus on comparing experimental and numerical predictions for fiber in a turbulent flow, we also recover a rigid to flexible transition regime previously observed in the numerical simulations of [20] and the study of [21].

We provide in fig. 10 the investigation of crossover regimes between flexible and rigid in the investigated range of flow and bending rigidity parameters. Fiber of different rigidities ranging from $K^b = 10^{-3}$ down to $K^b = 10^{-6}$ and length varying according to the required range of Sperm number were used in our simulations in order to investigate the evolution of the average squared end-to-end vector $\langle \mathbf{R}^2_{e,3D} \rangle_t$ with respect to the fiber initial length. We found that the decrease of fiber rigidity at constant turbulent intensity is equivalent to an increase of the turbulent intensity at constant elastic properties. Figure 10 shows the normalized $\langle \mathbf{R}^2_{e,3D} \rangle_t / L^2$ *versus* Sperm number $\mathtt{Sp}$ simulated for flows listed in table 1 and over a wide range of material property. Open symbols represent simulation results using 128^3 grid, blue and red crosses symbols are results of simulations using 512^3 grid. Experiments are represented by blue squares and the persistence length model is represented by the black dashed line. The prefactor γ in persistence length ($l_p = \gamma((EI)^{1/4}/(\mu\rho\epsilon)^{1/8})$) is found equal to 3 for the 128^3 and 512^3 simulations. The data are well described by the model and in good agreement with experiments with $\gamma = 2$. Hence, given the flow range and fibers properties, we both investigated configurations of slightly rigid and mostly flexible fibers. In all cases, fig. 9 shows that the definition of the persistence length is a relevant physical property to collapse all probability density functions of fiber curvature. The apparent flexible scaling behavior of the end-to-end length provided by fig. 10, might be explained by a smooth crossover to meet the quadratic regime expected for rigid fibers.

5 Conclusion

The buckling probability of an isolated fiber in Taylor-Green flow has been computed by means of numerical simulations. The results are in good agreement with the previous numerical and experimental studies of [13]. The buckling probability for $\mathtt{Sp} < 400$ is very close to the experimental data while some discrepancy occurs for $\mathtt{Sp} > 400$. This is a validation of the Gear Bead Model [15] in a complex flow composed of vortical and strain regions which are the ingredients of turbulence.

Based on the Gear Bead Model, we carried out numerical simulations of fibers deformation of various lengths and material properties in homogeneous isotropic turbulence. The bead model is coupled to direct numerical simulations of the Navier-Stokes equations. A tri-periodic domain containing sustained turbulence reproduces the basic features of a reference experiments to probe the different regime of fiber deformations, from short and rigid fibers to long and flexible filaments. We simulated two turbulent flows corresponding, respectively, to $\eta_K = 0.03$ (Flow I) and $\eta_K = 0.007$ (Flow II). Under these conditions the dimensionless length of the fiber L/L_g varies from 0.85 to 6.5 in Flow I and varies from 0.1 to 6 in Flow II. The range of variation covers the experimental conditions where L/L_g is of order unity. The end-to-end mean squared distance $\langle \mathbf{R}^2_{e,3D} \rangle_t$ has been obtained from numerical simulations as well as statistics on the fiber mean curvature. Both have been compared to experiments. The evolution of $\langle \mathbf{R}^2_{e,3D} \rangle_t$ shows a very good agreement between simulations and experiments with respect to the turbulent Sperm number $\mathtt{Sp} = \frac{L}{l_p}$ with $l_p = \gamma \frac{(EI)^{1/4}}{(\mu\rho\epsilon)^{1/8}}$. The results of a model inspired by polymer dynamics differ only by a prefactor $\gamma = 3$ for simulations and $\gamma = 2$ for experiments. The scaling proposed by [14] has been extended by varying independently the material property and length of the fiber showing that the balance between the turbulent fluctuation forcing for two turbulent flow fields and elastic bending holds over a much wider range of parameters than in experiments.

We only accounted for local hydrodynamic interactions between neighboring beads of the fiber without considering interactions over longer distances. Long-range hydrodynamic interactions might become important when the fiber is coiled or forming knots, *i.e.* when the length of fiber is very large. In the Taylor-Green vortices configuration, such complex shape filament has not been observed for the considered fiber aspect ratio in agreement with previously considered experiments. In the case of the turbulent flow, self-contact may occur only for very long flexible fibers but these events are very rare and we believe they do not flaw the statistics in the considered regimes. Finally, it is also interesting to mention that our model, as opposed to the one used in Rosti *et al.* (2018) takes care of short-range self-avoiding interactions of the chain. This is discussed in [21] and [20] showing that turbulence is responsible of a straightening, *i.e.* decreasing of the mean curvature, of long fibers.

Author contribution statement

MS carried out all the simulations, post-processing and analysis of the data. GV motivated the study and provided experimental results. PF was involved in the development of the Navier-Stokes parallel solver while BD, FP and EC have proposed the Gear Bead Model. All authors participated to physical analysis of the results and wrote the paper.

References

1. J.S. Guasto, R. Rusconi, R. Stocker, Annu. Rev. Fluid Mech. **44**, 373 (2012).
2. F. Lundell, L.D. Söderberg, P.H. Alfredsson, Annu. Rev. Fluid Mech. **43**, 195 (2011).
3. R. Cox, J. Fluid Mech. **45**, 625 (1971).
4. A. Meunier, J. Phys. II **4**, 561 (1994).
5. G.A. Voth, A. Soldati, Annu. Rev. Fluid Mech. **49**, 249 (2017).
6. C. Marchioli, M. Fantoni, A. Soldati, Phys. Fluids **22**, 033301 (2010).
7. D. Kunhappan, B. Harthong, B. Chareyre, G. Balarac, P. Dumont, Phys. Fluids **29**, 093302 (2017).
8. N.S. Berman, Annu. Rev. Fluid Mech. **10**, 47 (1978).
9. A. Robert, T. Vaithianathan, L.R. Collins, J.G. Brasseur, J. Fluid Mech. **657**, 189 (2010).
10. S. Jin, L.R. Collins, New J. Phys. **9**, 360 (2007).
11. E. Wandersman, N. Quennouz, M. Fermigier, A. Lindner, O. Du Roure, Soft Matter **6**, 5715 (2010).
12. Y.N. Young, M.J. Shelley, Phys. Rev. Lett. **99**, 058303 (2007).
13. N. Quennouz, M. Shelley, O. du Roure, A. Lindner, J. Fluid Mech. **769**, 387 (2015).
14. C. Brouzet, G. Verhille, P. Le Gal, Phys. Rev. Lett. **112**, 074501 (2014).
15. B. Delmotte, E. Climent, F. Plouraboué, J. Comput. Phys. **286**, 14 (2015).
16. L.J. Fauci, C.S. Peskin, J. Comput. Phys. **77**, 85 (1988).
17. V. Eswaran, S. Pope, Comput. Fluids **16**, 257 (1988).
18. E. Lauga, T.R. Powers, Rep. Prog. Phys. **72**, 096601 (2009).
19. M. Doi, S.F. Edwards, *The Theory of Polymer Dynamics*, Vol. **73** (Oxford University Press, 1988).
20. M.E. Rosti, A.A. Banaei, L. Brandt, A. Mazzino, Phys. Rev. Lett. **121**, 044501 (2018).
21. A. Gay, B. Favier, G. Verhille, EPL **123**, 24001 (2018).